Chemical Science

EDGE ARTICLE

Check for updates

Mechanistic insight of KBiQ$_2$ (Q = S, Se) using panoramic synthesis towards synthesis-by-design†

Rebecca McClain, [ID] [a] Christos D. Malliakas, [ID] [a] Jiahong Shen, [b] Jiangang He, [ID] [b] Chris Wolverton, [ID] [b] Gabriela B. González [ID] [c] and Mercouri G. Kanatzidis [ID] *[a]

Solid-state synthesis has historically focused on reactants and end products; however, knowledge of reaction pathways, intermediate phases and their formation may provide mechanistic insight of solid-state reactions. With an increased understanding of reaction progressions, design principles can be deduced, affording more predictive power in materials synthesis. In pursuit of this goal, *in situ* powder X-ray diffraction is employed to observe crystalline phase evolution over the course of the reaction, thereby constructing a "panoramic" view of the reaction from beginning to end. We conducted *in situ* diffraction studies in the K–Bi–Q (Q = S, Se) system to understand the formation of phases occurring in this system in the course of their reactions. Powder mixtures of K$_2$Q to Bi$_2$Q$_3$ in 1 : 1 and 1.5 : 1 ratios were heated to 800 °C or 650 °C, while simultaneously collecting diffraction data. Three new phases, K$_3$BiS$_3$, β-KBiS$_2$, and β-KBiSe$_2$, were discovered. Panoramic synthesis showed that K$_3$BiQ$_3$ serves an important mechanistic role as a structural intermediate in both chalcogen systems (Q = S, Se) in the path to form the KBiQ$_2$ structure. Thermal analysis and calculations at the density functional theory (DFT) level show that the cation-ordered β-KBiQ$_2$ polymorphs are the thermodynamically stable phase in this compositional space, while Pair Distribution Function (PDF) analysis shows that all α-KBiQ$_2$ structures have local disorder due to stereochemically active lone pair expression of the bismuth atoms. The formation of the β-KBiQ$_2$ structures, both of which crystallize in the α-NaFeO$_2$ structure type, show a boundary where the structure can be disordered or ordered with regards to the alkali metal and bismuth. A cation radius tolerance for six-coordinate cation site sharing of $\left(\frac{r^+}{r^{3+}}\right) \sim 1.3$ is proposed. The mechanistic insight the panoramic synthesis technique provides in the K–Bi–Q system is progress towards the overarching goal of synthesis-by-design.

[a]Department of Chemistry, Northwestern University, Evanston, Illinois 60208, USA. E-mail: m-kanatzidis@northwestern.edu

[b]Department of Materials Science and Engineering, Northwestern University, Evanston, Illinois 60208, USA

[c]Department of Physics, DePaul University, Chicago, Illinois, 60614, USA

Introduction

The discovery of new materials has led to revolutions in many scientific and technological fields, such as magnetism,[1] radiation detection,[2] optics,[3–6] superconductivity,[7,8] lithium-ion batteries,[9,10] thermoelectrics,[11] and phase-change memory.[12] Traditionally, materials discovery of inorganic structures involves exploratory synthesis to identify compounds using heuristically determined reaction conditions, where the compounds are isolated and identified upon completion of the reaction. Within this paradigm, it is unclear whether the desired products form upon heating, cooling, or while dwelling at maximum temperature, or if metastable, short-lived products appear and re-dissolve during the reaction. *In situ* diffraction techniques are a powerful tool that enable the observation of transient phases during the reaction in efforts towards materials discovery. Moreover, observing these transient phases leads to mechanistic understanding of the reaction; thereby advancing efforts to more rationally design or discover solid-state materials.[13–16] In particular, rational design is crucial to the pursuit of structural complexity for many fields, such as in thermoelectrics to achieve materials with lower thermal conductivity[17] and in nonlinear optics for large second harmonic generation.[5] To fully realize the potential for rational synthetic design, a comprehensive long-term approach to analyze solid-state reactions at all stages of the reaction is required.

A powerful tool that provides full awareness of phase identity and phase evolution during a reaction is *in situ* powder X-ray diffraction. This technique enables the direct observation of all crystalline phases, including intermediate ones, during a solid-state synthesis.[18,19] This "panoramic" view of the phase

space explored during the reaction enables an understanding of the reaction pathway required to form the final products. To this end, *in situ* powder X-ray diffraction promotes the discovery of new materials and increased mechanistic understanding of solid-state chemistry.

However, simply conducting *in situ* powder X-ray diffraction on systems in isolation is not sufficient to achieve the generalized understanding of solid-state reaction dynamics necessary to maximize the potential for discovery. Comprehensive studies of multiple closely related compositions and systems are needed to paint a full picture of reactions that can then be extended to new systems. Therefore, the aggregation of mechanistic data describing material formation and progression of intermediate phases is the first step to determining reaction pathways for rational synthesis.[13,14,20–24] This technique must therefore be applied to a broad, diverse set of systems and phases spaces. Once these reaction pathways of these systems are cataloged and codified, they can be data mined for design principles among similar reaction types.[13] With reaction types and assembly rules, predictive power of material synthesis can be achieved, leading to intentional synthesis of targeted materials with chosen, desired properties.[25]

In situ powder X-ray diffraction has been utilized for various interests such as materials discovery[18,19,26] and mechanism elucidation,[25,27–33] as well as the investigation of metathesis reactions,[27,34] self-propagating high temperature syntheses,[14,25,28] phase change,[14,35] decomposition,[36] and crystallization.[14,25,28] This approach has shown success in discovering new materials, even in systems that were previously investigated.[18,19] Furthermore, it has been shown that, by using mechanistic insight from *in situ* studies, the reaction pathway can be influenced.[30] Studies focused on building a database of reaction formation and mechanistic understanding for a specific reaction type can be combined in aggregate towards the goal of rational synthesis.

A promising phase space to study is in the A–Pn–Q systems, where A is an alkali metal, Pn is a pnictogen such as bismuth or antimony, and Q is a chalcogenide,[37,38] as many are reported structures and have been of interest for their thermoelectric[39–45] and optical[5,35,46,47] properties. Moreover, a number of the known compounds are isostructural disordered analogues, such as $KBiS_2$, $NaBiS_2$, $NaBiSe_2$, $KBiSe_2$, and $NaSbS_2$, while ordered phases contain similar structural motifs.[48–50] Investigation of this family of structures expands the library of known materials, reaction pathways, and understanding of structure–property relationships. Reaction pathways can then be compared within this phase space to understand their design principles. The combination of experimental observation and computational data-mining can accelerate materials discovery and expedite the development of the mechanistic understanding required to achieve rational synthesis of materials.[23,51]

Herein, we have applied this *in situ* diffraction technique using both in-house and synchrotron sources to the K–Bi–S and K–Bi–Se system, by monitoring the reaction between the respective binaries, K_2Q and Bi_2Q_3 (Q = S, Se). Powder mixtures were heated to 800 °C or 650 °C, while diffraction data was simultaneously collected. From this investigation, we found

that the two systems share an isostructural intermediate phase, K_3BiQ_3. The presence of this intermediate phase in both reactions suggests K_3BiQ_3 is mechanistically important for $KBiQ_2$ formation from the binary starting materials. Two additional compounds were discovered: β-$KBiS_2$ and β-$KBiSe_2$. These compounds crystallize in the α-$NaFeO_2$ structure type and are cation-ordered polymorphs of the known rocksalt ternaries. The ability of $KBiQ_2$ to form both a disordered and ordered phase, while $NaBiQ_2$ and $RbBiQ_2$ crystallize in the rocksalt and α-$NaFeO_2$ type structures, respectively, suggests that there is a cation radius tolerance $\left(\dfrac{r^+}{r^{3+}}\right)$ of 1.33 or greater for high symmetry rocksalt formation. This work is one of the pioneer studies in proposing a tolerance factor for a chalcogenide system.[52–54] We have also performed density functional theory (DFT) calculations to show that the cation-ordered β-$KBiQ_2$ polymorphs are thermodynamically stable and demonstrated that DFT can be used as a complimentary tool in the panoramic studies to determine the phase stabilities.

Experimental section

Reagents

Chemicals in this work were used as-obtained: bismuth metal (99.99%, American Elements), sulfur, (sublimed, 99.99%, Spectrum), selenium pellets (99.99%, American Elements), potassium metal (99.5%, Aldrich), glassy carbon (99.9%, Aldrich). K_2S and K_2Se were synthesized using stoichiometric amounts of the elements in liquid ammonia as described elsewhere.[47]

Synthesis

Bismuth sulfide, Bi_2S_3. A 1.1226 g amount (0.035 mol) of elemental sulfur was combined with 4.8774 g (0.023 mol) of bismuth shots in a 9 mm (O.D.) fused silica tube. The tube was flame sealed under vacuum (10^{-3} mbar). The sample was heated to 500 °C in 24 hours and soaked for 24 hours before furnace cooling.

Bismuth selenide, Bi_2Se_3. A 2.7104 g amount (0.028 mol) of elemental selenium was combined with 3.8296 g (0.018 mol) of bismuth shots in a 9 mm (O.D.) fused silica tube. The tube was flame sealed under vacuum (10^{-3} mbar). The sample was heated to 850 °C in 8.5 hours and soaked for 12 hours, then cooled to 450 °C in 8 h. The sample was annealed at this temperature for 48 hours to minimize selenium vacancies. The sample was then furnace cooled. The sample was ball milled in a Retsch Mixer Mill MM 200 at 20 rps with 20 balls for an accumulative 2.5 hours.

β-$KBiS_2$. K_2S (0.071 g, 0.64 mmol) and Bi_2S_3 (0.329 g, 0.64 mmol) were mixed in a mortar and pestle and transferred in a N_2 glovebox to a carbon coated 9 mm (O.D.) fused silica tube, which was flame sealed under vacuum (10^{-3} mbar). The sample was heated to 875 °C in 12 h and soaked for 3 h, then cooled to 775 °C in 16 hours before furnace cooling. Powder X-ray diffraction (PXRD) shows that the sample is bulk phase pure.

K₃BiS₃. K_2S (0.157 g, 1.4 mmol) and Bi_2S_3 (0.243 g, 0.47 mmol) were mixed in a mortar and pestle in a N_2 glovebox. The mixture was transferred to a carbon coated 9 mm (O.D.) fused silica tube and flame sealed under vacuum (10^{-3} mbar). The sample was heated to 450 °C in 6 h and soaked for 192 h before furnace cooling. The sample was rehomogenized using a mortar and pestle in an N_2 glovebox, then subsequently annealed at 450 °C for 48 hours; Rietveld refinement of the sample reveals a 7.7(2) wt% impurity of α-KBiS₂.

β-KBiSe₂. K_2Se (0.077 g, 0.49 mmol) and Bi_2Se_3 (0.0323 g, 0.49 mmol) were added to a carbon coated 9 mm fused silica tube, which was flame sealed under vacuum (10^{-3} mbar). The sample was heated to 800 °C in 9 h and soaked for 30 minutes before cooling to 575 °C in 72 h. The sample was then cooled to 475 °C in 96 h before furnace cooling. Phase purity confirmed using PXRD.

Physical measurements

***In Situ* powder X-ray diffraction.** A STOE STADI MP high-resolution diffractometer with an oven attachment (STOE HT) were used to collect temperature-dependent data. The diffractometer was equipped with an asymmetric curved germanium monochromator and one-dimensional silicon strip detector (MYTHEN2 1K from DECTRIS). The starting materials were sieved (<45 μm), mixed, and diluted using glassy carbon. Dilutions were required to mitigate sample attenuation of the X-ray beam and, therefore, optimize the signal-to-noise ratio of the diffraction measurement. Samples were then packed into 0.3 mm diameter quartz capillaries, which were flame sealed under vacuum (*ca.* 3.0×10^{-3} mbar). All capillaries were carbon coated to prevent glass attack. Ground fused silica was used as a spacer at the tip of the capillary, where the capillary was re-sealed and bare of carbon coating. Diffraction data was collected every 15 °C using pure-Cu Kα1 radiation (1.54056 Å) operated at 40 kV and 40 mA for the sulfide system and pure-Mo Kα1 radiation (0.70930 Å) operated at 50 kV and 40 mA for the selenide system. Samples were heated to 800 °C or 650 °C with a heating rate of 4°C min^{-1} and a dwell time at max temperature of 90 minutes. Temperature stability is typically 0.1 °C. Samples were spun during collection. The instrument was calibrated against a NIST Silicon standard (640d) prior the measurement.

***Ex situ* powder X-ray diffraction.** X-ray powder diffraction patterns were collected on a Rigaku Miniflex600 diffractometer with Cu Kα1 radiation (1.5406 Å) operating at 40 kV and 15 mA with a high-speed silicon strip detector. A zero-background silicon sample holder with 0.2 mm × 4 mm well was used. Visualization of the crystal structures was done with Vesta software.[55]

PXRD data used for K₃BiS₃ Rietveld refinement was collected at room temperature on a STOE-STADI-P powder diffractometer equipped with an asymmetric curved germanium monochromator (pure-CuKα1 radiation, $λ = 1.54056$ Å) and one-dimensional silicon strip detector (MYTHEN2 1K from DECTRIS). The line focused Cu X-ray tube was operated at 40 kV and 40 mA. Powder was packed in a 3 mm metallic mask and sandwiched between two polyimide layers of tape. Intensity data from 3 to 124° 2θ were collected over a period of 45 min. The instrument was calibrated against a NIST Silicon standard (640d) prior to the measurement.

High resolution synchrotron powder diffraction data were collected using beamline 11-BM at the Advanced Photon Source (APS), Argonne National Laboratory using an average wavelength of 0.4577 Å. Discrete detectors covering an angular range from 2 to 24° 2θ are scanned over a 6° 2θ range, with data points collected every 0.001° 2θ and scan speed of 0.01° s^{-1}.

Pair distribution function measurements and analysis. Kapton capillaries (0.8 mm diameter) were filled with sieved powder samples (<45 μm) inside a glovebox. X-ray scattering data for α-KBiQ₂ (Q = S, Se) samples were collected at Sector 11-ID-B of the Advanced Photon Source at Argonne National Laboratory using an incident wavelength of 0.143 Å, up to a Q_{max} of 36.4 Å^{-1}. The sample-to-detector distance was approximately 175 mm for the sulfide, resulting in a Q_{max} of 36.4 Å^{-1}. The sample-to-detector distance for the selenide was approximately 250 mm, resulting in a Q_{max} of 29.1 Å^{-1}.

GSAS-II was used to calibrate the sample-to-detector distance, detector alignment, and instrumental resolution parameters using a NIST CeO₂ standard and to integrate the data (ref. 56). The empty Kapton capillary signal was subtracted from each scattering data pattern using PDFgetX3[57] prior to obtaining the Pair Distribution Functions (PDFs). PDFgui[58] was used to fit PDFs in the range 2 Å < r < 30 Å. Subgroups were generated using the Bilbao Crystallographic Server;[59–61] space groups investigated included $R\bar{3}m$, $Pm\bar{3}m$, $C2/m$, $P\bar{3}m1$, $I4/mmm$, $Pn\bar{3}m$, $P3_221$.

Optical measurements. Optical diffuse reflectance measurements were made at room temperature with a Shimadzu UV-3600 PC double-beam, double-monochromator spectrophotometer. The measurement of diffuse reflectivity can be used to obtain values for the band gap from a powder sample at room temperature. BaSO₄ powder was used as a reference. The reflectance data was converted to absorbance using the Kubelka–Munk equation: $α/S = (1 − R)2/2R$. R is the reflectance at a given wavelength, $α$ is the absorption coefficient, and S is the scattering coefficient. Valence band maximum energy (VBM) was measured by photoemission spectroscopy in air on a Riken-Keiki PESA AC-2. Samples are scanned under ambient conditions using UV light (4.20–6.20 eV). The number of photoelectrons generated at each excitation energy is measured and the VBM is the onset of the PESA spectra, as photoelectrons are only generated when the photon energy is higher than the VBM energy. Conduction band minimum energies are found by subtracting the optical band gap from the VBM energy.

Differential thermal analysis. Differential thermal analysis (DTA) was performed using a Netzsch STA 449 F3 Jupiter simultaneous thermal analysis (STA) instrument. Samples were loaded into carbon-coated fused silica tube and flame-sealed under vacuum (*ca.* 3×10^{-3} mbar). Samples were heated to 900 °C, cooled to 200 °C, then heated once more to 900 °C, before cooling to room temperature. The rate for cooling and heating was set to 7.5 °C min^{-1}.

Computational methods

All DFT calculations are performed using the projector augmented wave (PAW) method,[62,63] as implemented in the Vienna *Ab initio* Simulation Package (VASP).[64,65] The Perdew–Burke–Ernzerhof (PBE) exchange–correlation functional[66] and a plane wave basis set with a cutoff energy of 520 eV were used. A Γ-centered k-mesh with ≈ 8000 k-points per reciprocal atom (KPPRA) was used to sample the Brillouin zone. The Open Quantum Material Database (OQMD)[51,67] was used for convex hull construction. To calculate the formation energy of the cation-disordered $KBiQ_2$ $Fm\bar{3}m$ structures, a 32-atom special quasi-random structure (SQS)[68] was generated by using the Monte Carlo algorithm (mcsqs) as implemented in the Alloy Theoretic Automated Toolkit (ATAT).[69,70] The cluster correlations used to define the SQS were specified using a distance-based cutoff of all 2-, 3-, and 4-body clusters with a maximum distance of 5–6 Å. To calculate the effective band structure of the K/Bi disordered cubic phase ($Fm\bar{3}m$), a $2 \times 2 \times 2$ supercell was generated based on the perfect rocksalt structure with bismuth and potassium alternatively stacking along the [111] direction. The potassium and bismuth atoms are then randomly distributed in the supercell to simulate the cation-disordered $KBiQ_2$ $Fm\bar{3}m$ structures. Effective band structures were recovered from the supercell calculations using the band unfolding technique proposed by Medeiros *et al.*[71,72]

Results and discussion

Panoramic synthesis KBiS$_2$

The synthesis of KBiS$_2$ has been previously reported using potassium carbonate, elemental bismuth, and elemental sulfur.[48,73] KBiS$_2$ crystallizes in the simple rocksalt structure,[48,73] where potassium and bismuth have equivalent occupancy in the sodium site and sulfur is in the chloride site. Moreover, the K–Bi–S phase space is of interest for thermoelectric materials[74] and photovoltaics,[75] in efforts towards rational design within this phase space, we began with this simple structure.

To monitor the reaction progression in the K–Bi–S system, panoramic syntheses were conducted using a commercial STOE high-temperature furnace (HT) attachment for a STOE STADI-MP powder X-ray diffractometer. In previously reported syntheses, an excess of potassium starting material was used to form KBiS$_2$, therefore a ratio of 1.5 K$_2$S : 1 Bi$_2$S$_3$ is used.[73] The reaction has a maximum temperature of 800 °C. The overlaid diffraction patterns from the panoramic synthesis are shown in Fig. 1A. Phases are identified primarily through pattern matching. A schematic of the reaction pathway with relative mole fractions of the phases is shown in Fig. 1B. The relative mole fraction of the starting material amorphous K$_2$S was determined according to the experimental loading of the material. It is useful to regard the reaction between K$_2$S and Bi$_2$S$_3$ as a Lewis acid–base reaction in which K$_2$S is the base and Bi$_2$S$_3$ is the acid. In this context, basic activity increases with the K$_2$S fraction and acidic activity increases with the Bi$_2$S$_3$. The end crystalline products are KBiS$_2$ and cristobalite, a high temperature polymorph of SiO$_2$. The ground amorphous silica, which
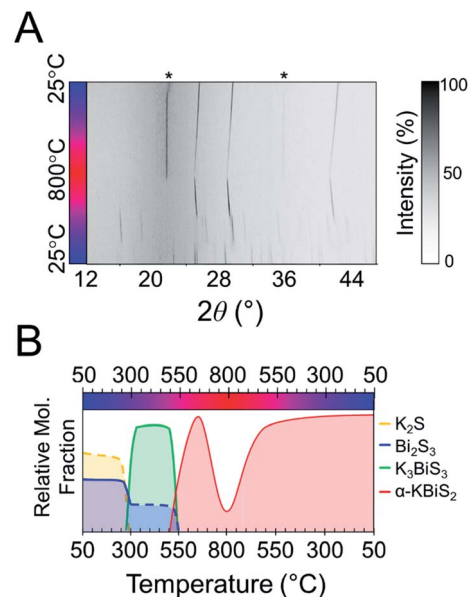

Fig. 1 (A) Heat map of 1.5 K$_2$S + 1 Bi$_2$S$_3$. Asterisks indicate observed peaks from cristobalite formation. (B) Reaction map of 1.5 K$_2$S + 1 Bi$_2$S$_3$. Relative compositions are shown; dashed lines represent an amorphous phase.

was used as a spacer to protect the glass tip of the capillary, crystallized after reaching temperatures above 700 °C. To avoid this, all subsequent panoramic syntheses in this system have a maximum temperature of 650 °C. An intermediate phase is observed during the reaction, appearing at 270 °C and disappearing at 510 °C as the product, KBiS$_2$, emerges. The intermediate phase was isolated *ex situ* as described in the Experimental section and determined to be K$_3$BiS$_3$ *via* Rietveld refinement (Fig. S1 and Tables S1–S4†).

The intermediate phase, K$_3$BiS$_3$, shown in Fig. 2, crystallizes in the cubic Na$_3$AsS$_3$ structure type (space group $P2_13$; $a = b = c = 9.4425(1)$ Å) and is isostructural to K$_3$SbS$_3$ and Na$_3$SbS$_3$.[76] The formation of an intermediate phase of this composition is surprising because it implies a reaction of K$_2$S and Bi$_2$S$_3$ in a 3 : 1 ratio, which is a more basic condition than what is being used in this reaction, where the ratio is 3 : 2. This suggests that K$_3$BiS$_3$ is a kinetic product.

K$_3$BiS$_3$ has two structural motifs: trigonal-pyramidal BiS$_3$ units and distorted octahedral KS$_6$ units. The isolated pyramidal molecule of $[BiS_3]^{3-}$ makes the structure of K$_3$BiS$_3$ essentially molecular. We synthesized this intermediate *ex situ* using the conditions identified by the panoramic synthesis experiments and refined its structure using Rietveld refinement (Fig. S1†). The trigonal-pyramidal units of BiS$_3$ have bond lengths and bond angles of 2.593(7) Å and 99.2(3)°, respectively. The distorted KS$_6$ octahedra exhibit three different coordination environments, shown in different colors in Fig. 2B. The distortion of the octahedra give rise to a range of bond lengths between 3.11(2) and 3.53(1) Å. The distorted octahedra of K1, shown in blue, is capped by a bismuth and shares a corner with the three other BiS$_3$ units in the structure. K2, in turquoise, is
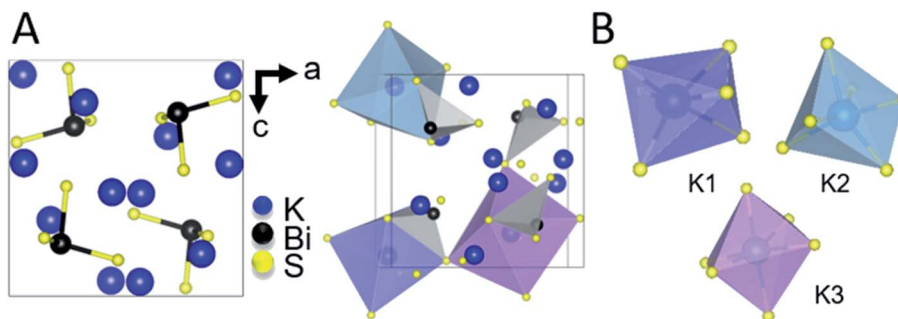
Fig. 2 (A) Ball and stick representation of K_3BiS_3 (left) and an illustration of the three different octahedra of KS_6 and all BiS_3 units (right). (B) Isolated representations of the KS_6 distorted octahedra.

edge-sharing with three BiS_3 units, while K3, shown in purple, is exclusively corner-sharing with the BiS_3 polyhedra.

By comparing the structures in the 1.5 K_2S + Bi_2S_3 reaction, shown in Fig. 3, the role of K_3BiS_3 as an intermediate phase in the formation of $KBiS_2$ is examined. The coordination environment of potassium can be described as a gradual progression from tetrahedral to octahedral. In the starting material, the potassium cation begins in the K_2S anti-fluorite structure consisting of KS_4 tetrahedra with bond lengths of 3.191 Å,[77] and over the course of the reaction expands to the distorted KS_6 octahedra in K_3BiS_3. By the final product, potassium forms ideal KS_6 octahedra in $KBiS_2$. Of note, the K–S bond lengthens in K_3BiS_3, before shortening to 3.02 Å in the final $Fm\bar{3}m$ structure.[78] In contrast, the bismuth coordination sphere does not undergo a gradual progression. In fact, bismuth undergoes an unexpected decrease in coordination number from square pyramidal and distorted octahedral to trigonal pyramidal, before transitioning to octahedral in $KBiS_2$. In K_3BiS_3, bismuth stereochemically expresses its lone pair into a void created by the potassium cations, then no longer expresses its

lone pair in the final product, $KBiS_2$. The bismuth precursor, Bi_2S_3, contains square-pyramidal BiS_5 units and distorted BiS_6 octahedra, as illustrated in Fig. 3. Three different Bi–S bond lengths are present in the BiS_5 units. The bond lengths in the basal plane are divided equally between 2.74(1) and 2.96(1) Å, while the apical Bi–S in BiS_5 is the shortest bond length in the structure at 2.56(1) Å.[77] The BiS_6 octahedra has two bond lengths at 2.67(1) Å, another two at 2.96(1) Å, as well as one at 3.05(1) and 2.69(1) Å. The Bi–S bond length shortens to 2.62(1) Å in K_3BiS_3, before increasing to 3.02 Å in $KBiS_2$. A concurrent shortening of the Bi–S bonds and lengthening of the K–S bonds in K_3BiS_3 is likely a result of the concomitant separation of the Bi_2S_3 chains and incorporation of the KS_4 units. Owing to its utility as a structural transition framework, K_3BiS_3 therefore can be considered a structural intermediate for the formation of $KBiS_2$.

To explore if the formation of rocksalt $KBiS_2$ persists, an increase in amount of Bi_2S_3 relative to K_2S was investigated. The overlaid diffraction patterns and reaction map of the 1 K_2S : 1 Bi_2S_3 panoramic synthesis are shown in Fig. 4A and B,
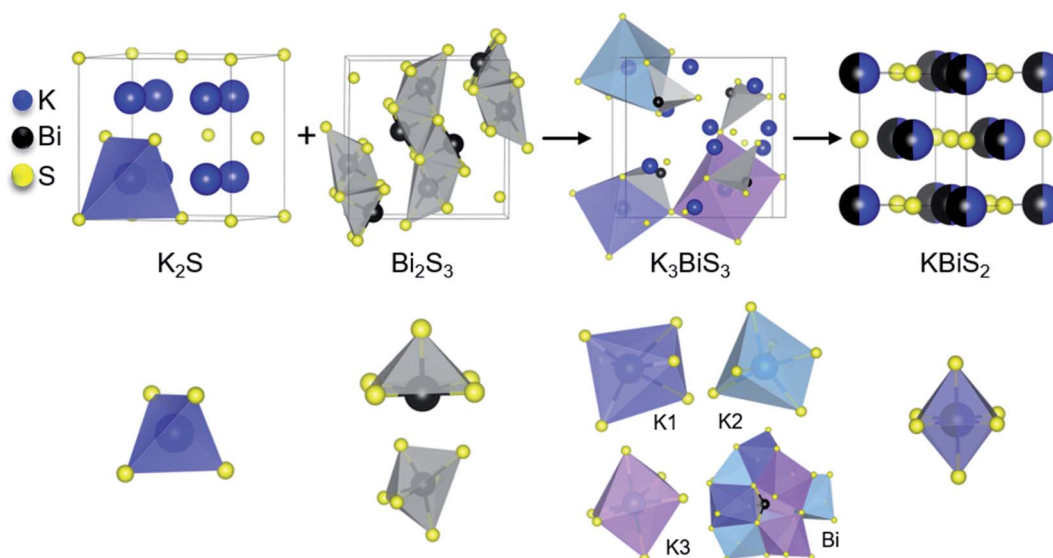

Fig. 3 Reaction progression of the starting materials, K_2S and Bi_2S_3, to $KBiS_2$ through the intermediate phase K_3BiS_3. Unique cation coordination environment is shown for each structure. A bismuth atom in K_3BiS_3 is shown within the cavity formed by the KS_6 distorted octahedra.
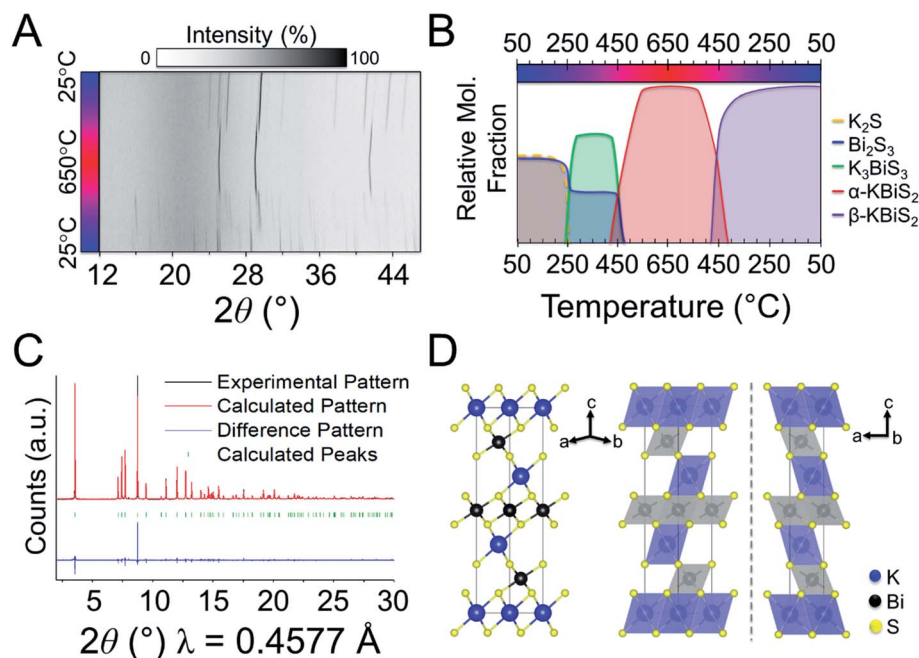
Fig. 4 (A) Overlaid diffraction patterns of 1 K_2S + 1 Bi_2S_3. (B) Reaction map of 1 K_2S + 1 Bi_2S_3. Nominal compositions are shown; dashed lines represent a noncrystalline phase. (C) Structure solution for β-$KBiS_2$. (D) Structural representation of the ordered rocksalt, β-$KBiS_2$.

respectively. As before, K_3BiS_3 forms first and appears between 240–250 °C, which is similar to the formation temperature of 270 °C in the K_2S-rich reactions featuring a ratio of 1.5 : 1. The continued formation of K_3BiS_3 before the crystallization of $KBiS_2$, despite a different final product, corroborates that this kinetic intermediate is mechanistically important for the formation of the rocksalt structure. The $KBiS_2$ rocksalt structure emerges at *ca.* 435 °C. The rocksalt phase persists through the maximum temperature and, on cooling, a third phase is observed starting between 465–480 °C. $KBiS_2$ persists until approximately 300 °C on cooling, where the third phase is the sole final product.

The third and final phase in this reaction is a cation-ordered polymorph of $KBiS_2$ in the rhombohedral α-$NaFeO_2$ structure type ($R\bar{3}m$, $a = b = 4.12983(3)$ Å, $c = 22.09484(17)$ Å). The structure of the $KBiS_2$ polymorph, hereafter named β-$KBiS_2$, was determined using Rietveld refinement on synchrotron PXRD data (Fig. 4C). β-$KBiS_2$ is an ordered rocksalt that is isostructural to $RbBiS_2$.[79] In this structure type, cation trigonal anti-prisms are connected through edge-sharing as in the disordered rocksalt structure (Fig. 4D).[80] The layers alternate between $CdCl_2$-type $[BiS_2]^-$ layers and potassium cations. It is notable that the ordered $R\bar{3}m$ forms only when stoichiometric amounts of bismuth and potassium precursors are used; an excess of just 5% of K_2S yields the rocksalt structure (Fig. S3†). The original synthesis for the cation-disordered $Fm\bar{3}m$ $KBiS_2$ (now called α-$KBiS_2$) also uses an excess of the potassium precursor, K_2CO_3.[73] This suggests that an excess of potassium may have a role in destabilizing the lower symmetry structure.

Thermal analysis data of β-$KBiS_2$ shown in Fig. S5† and Density Functional Theory (DFT) calculations, described further

below, corroborate the experimental evidence that cation-ordered β-$KBiS_2$ is the thermodynamically stable phase. The endothermic peak at *ca.* 480 °C upon heating and broad exothermic peak at *ca.* 405 °C upon cooling in the thermal analysis data indicate β-$KBiS_2$ undergoes a phase transition. The temperature of these peaks corresponds to the transition temperature for the α-$KBiS_2$ to β-$KBiS_2$ transition in Fig. 4A. This, in conjunction with the identity of the post-thermal analysis product as β-$KBiS_2$, confirms these signals result from phase transitions from a low to high temperature phase. Moreover, DFT calculations show that cation-ordered β-$KBiS_2$ sits on the convex hull and, thus, is the thermodynamically stable phase, while cation-disordered α-$KBiS_2$ sits at 75 meV per atom above the convex hull (*i.e.* above β-$KBiS_2$).

Panoramic synthesis of $KBiSe_2$

$KBiSe_2$ is reported to crystallize in the rocksalt structure and was hypothesized to proceed through a similar mechanism to α-$KBiS_2$ owing to their isostructural nature. The panoramic synthesis on 1 K_2Se + 1 Bi_2Se_3 was conducted and is illustrated in Fig. 5. Different colors are used to highlight different phases that form during the reaction, beginning with the starting materials in blue. At 195 °C, again the analogous material, K_3BiSe_3, forms (Fig. S6;† $P2_13$; $a = b = c = 9.773(2)$ Å).[49] The appearance of K_3BiSe_3 (indicated in green) as an intermediate phase also in the selenide analogue reaction supports that this molecular salt phase may be important mechanistically to the reaction path.

The reaction selectivity of K_3BiQ_3 (Q = S, Se) directly proceeding the formation of the $KBiQ_2$ ternary is postulated to be structural in origin as opposed to energetic. *In situ* studies
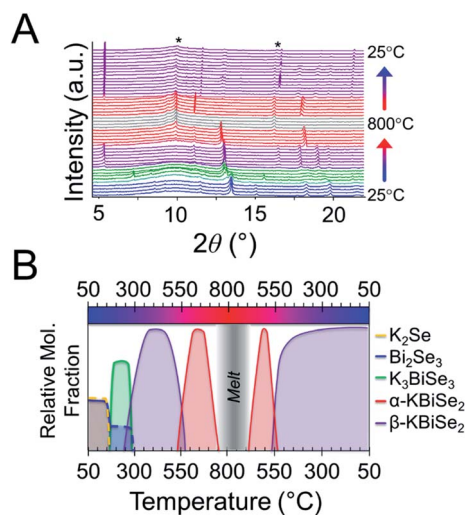
Fig. 5 (A) Overlaid diffraction pattern for K_2Se + Bi_2Se_3 panoramic synthesis. Asterisks indicate cristobalite (SiO_2) crystallization. (B) Reaction map of 1 K_2Se + 1 Bi_2Se_3. Nominal compositions are shown; dashed lines represent a noncrystalline phase.

observing the phase formation found the composition of the first transient phase to be that which yielded the largest energy release[81] or the fastest energy release.[30] The former does not apply for these chalcogenide systems as the formation of K_3BiQ_3 is less energetically favorable than the β-$KBiQ_2$ phases. Specifically, the formation energies of K_3BiS_3 and K_3BiSe_3 are calculated to be −48 meV per atom and −28 meV per atom below the convex hull, respectively, while those of β-$KBiQ_2$ are −68 meV per atom and −60 meV per atom below the hull for the sulfide and selenide, respectively. The alpha phases have positive formation energies relative to the convex hull according to DFT calculations and are, therefore, considered unstable. K_3BiQ_3 also does not provide the fastest energy release as diffusion must occur for this phase to form as compared to $KBiQ_2$. The precursor loadings in this work are 3 K_2S : 2 Bi_2S_3 (e.g. 1.5 : 1) and 1 K_2Q : 1 Bi_2Q_3 (Q= S, Se). The precursors were sieved and thoroughly mixed, such that the average contact between particles are expected to mirror that of the loading ratio. Correspondingly, no notably K_2Q-rich or poor areas are expected. The fastest energy release would therefore be the formation of $KBiQ_2$, however, K_3BiQ_3 reproducibly forms first in both chalcogenide system regardless of loading ratio. The formation of the K_3BiQ_3 structural intermediate therefore cannot be easily rationalized by current thermodynamic or kinetic theories. However, the formation of the potassium-rich intermediate, persistent even in relatively potassium-poor reactant loading, underscores that this compound is necessary for the formation of the $KBiQ_2$ ternary in these conditions.

The structural intermediate, K_3BiSe_3, shown in green in Fig. 5, persists until a new phase emerges at 285 °C, shown in purple. This new phase disappears at 555 °C before reappearing at 525 °C on cooling as the final product. This phase is isostructural to β-$KBiS_2$ and hereafter called β-$KBiSe_2$ ($R\bar{3}m$, $a = b = 4.26442$ (1) Å, $c = 23.0290$(1) Å). When β-$KBiSe_2$ disappears, the

known rocksalt structure-type α-$KBiSe_2$ begins to emerge. Upon cooling, β-$KBiSe_2$ reappears by 500 °C. In order to isolate α-$KBiSe_2$, the product was quenched at 650 °C and annealed. Attempts to synthesize α-$KBiSe_2$ using the binaries without quenching, even with an excess of K_2Se, were unsuccessful.

The overall reaction pathway in the selenide and sulfide systems is similar. Both systems proceed through a K_3BiQ_3 (Q = S, Se) intermediate. The coordination sphere of potassium increases from an anti-fluorite tetrahedron to distorted octahedra in K_3BiSe_3, as it does in the sulfide system. The coordination sphere of bismuth in the selenide system, however, decreases during the intermediate phase from an octahedron in Bi_2Se_3, shown in Fig. S7,† to trigonal pyramidal in the discrete ions in K_3BiSe_3, before returning to an octahedron in both the highly dense ordered and the disordered rocksalt type $KBiSe_2$. The formation temperature of the selenide ternaries is observed lower than that of the sulfide likely as a result of the lower melting points of the selenide binaries, the higher basicity of K_2Se than K_2S, and the more polarizable anionic framework of the selenium ternary, which facilitates ion mobility.[82] Similar to the $KBiS_2$ system, thermal analysis (Fig. S8†) and DFT calculations show that the ordered, α-$NaFeO_2$ type polymorph of $KBiSe_2$ is the thermodynamically stable phase. Comparable to its sulfur analogue, cation-disordered α-$KBiSe_2$ sits 76 meV per atom above the ordered, stable β-$KBiS_2$ phase.

Investigation of local structure

Local off-centering from ns^2 lone pairs has been demonstrated previously for materials containing heavy main-group elements as for example the emphanisis effects in PbQ.[83–88] The structure of the titular $KBiQ_2$ compounds is therefore expected to be locally distorted as a result of stereochemical activity of the Bi^{3+} lone pair, while the global structure remains in the rocksalt or α-$NaFeO_2$ structure type for the alpha and beta phases, respectively. Pair distribution function (PDF) analysis confirms that the data are well fit using $Fm\bar{3}m$ for α-$KBiS_2$ and α-$KBiSe_2$ at long r ranges (Fig. 6A and E). However, the split of the first PDF peak is not well fit, as shown in Fig. 6C and G. The Bilbao Crystallographic Server[59–61] was used to generate possible subgroups of space group $Fm\bar{3}m$ assuming the Wyckoff positions $4a$ and $8c$. Those subgroups were used to fit the PDF data. The short range ($r < 6$ Å) were better fit using the lower symmetry space group $P2_13$ with partial site occupations in a cubic lattice cell as shown in Fig. 6B, D, F, and H. The split in the first coordination shell was better modeled by off-centering the atoms from the ideal rocksalt positions as illustrated in Fig. 6I and J.

Optical properties of α- and β-$KBiQ_2$

As the ratio of K_2Q to Bi_2Q_3 becomes stoichiometric in the syntheses, the final product transitions from α-$KBiQ_2$ to β-$KBiQ_2$ with band gap energies of 0.84(2) eV and 1.09(2) eV, respectively, for the selenides (red, Fig. 7A) and 1.23(2) eV and 1.55(2) eV for the sulfides (blue, Fig. 7A). As the compounds undergo a decrease in symmetry moving from the disordered α-$KBiQ_2$ to the ordered β-$KBiQ_2$, we observe a subsequent increase in band gap. The dimensional reduction from the ordering of β-
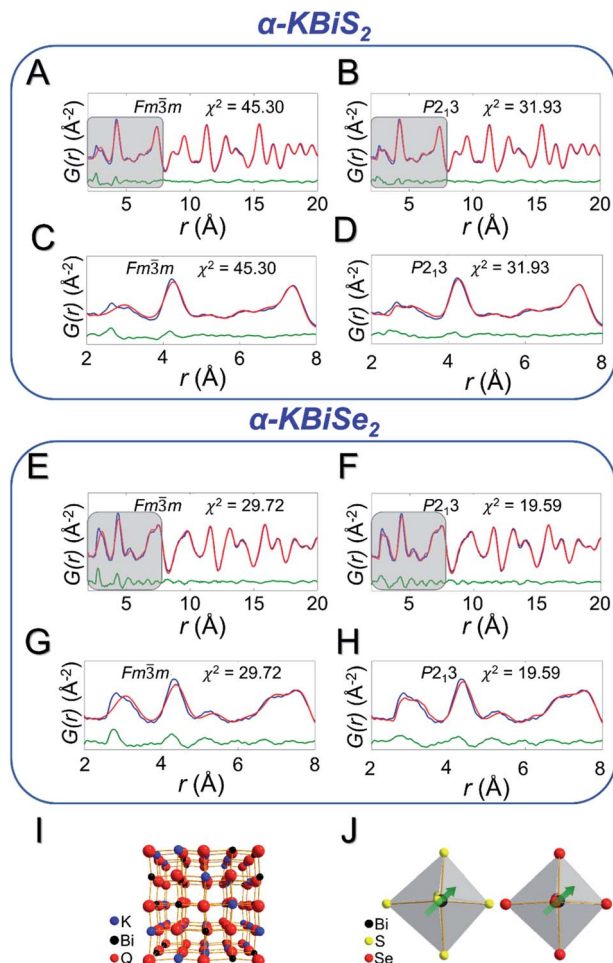
α-KBiS₂

α-KBiSe₂

Fig. 6 PDF fits for α-KBiS₂ using a (A) $Fm\bar{3}m$ model and (B) $P2_13$ model. These models are zoomed in to the short range ($r < 8$ Å), highlighted in grey, for the $Fm\bar{3}m$ model (C) and for the $P2_13$ model (D). In the PDF fits, red is the calculated PDF pattern, blue is the experimental data, and green is the difference pattern. PDF fits for α-KBiSe₂ using a (E) $Fm\bar{3}m$ model and (F) $P2_13$ model; zoomed in region shown for the $Fm\bar{3}m$ model (G) and for the $P2_13$ model (H). (I) Shows a 2 × 2 × 2 unit cell representation of KBiQ₂ and (J) highlights the off-centering of bismuth in the $[BiS_6]^{3-}$ and $[BiSe_6]^{3-}$ octahedra.
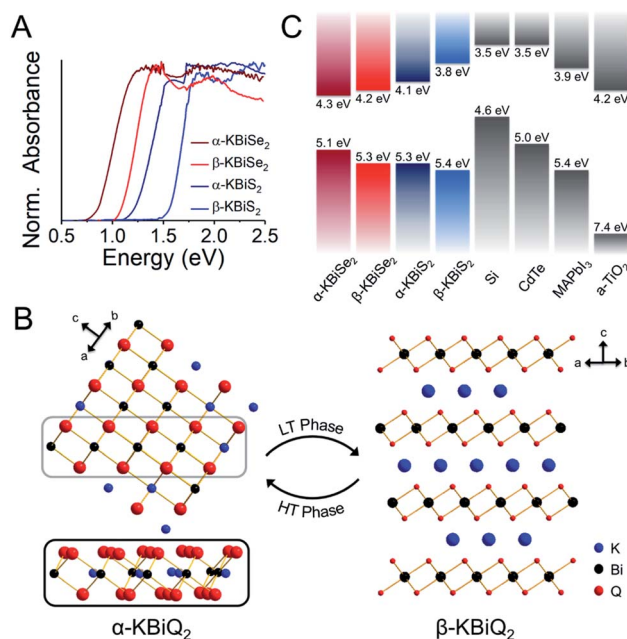

Fig. 7 (A) Experimental band gaps for the known α-KBiQ₂ ($Fm\bar{3}m$) and discovered β-KBiQ₂ phases ($R\bar{3}m$). (B) Illustration of dimension reduction from the 3D covalent framework in the high temperature (HT) phase, α-KBiQ₂, to the layered 2D covalent framework in the low temperature (LT) phase, β-KBiQ₂. For both structures, only covalent bonds (e.g. Bi–Q bonds) are shown. The site distribution of bismuth and potassium in α-KBiQ₂ was randomized, while constrained to maintain equivalent amounts of the cations. The inset for α-KBiQ₂ tilts the indicated portion of the structure to highlight the 3D connectivity through the plane. (C) Depiction of valence band maxima, conduction band minima, and band gap energies for α-KBiQ₂, β-KBiQ₂, Si,[90,91] CdTe,[92] MAPbI₃,[93] and TiO₂ (anatase).[94,95]

KBiQ₂ into layers of $[BiQ_2]^-$ and K⁺ (Fig. 7B) yields a blue shift in the experimental band gap, as similarly observed for other semiconductors.[84,89] Fig. 7C shows the energies of the valence band maxima for α-KBiQ₂ and β-KBiQ₂ measured using a Kelvin Probe (see Experimental section) as well as for four well-known semiconductors (Si, CdTe, methylammonium lead iodide (MAPbI₃), and TiO₂) for reference. The energies of the conduction band minima are included and were extrapolated using the valence band maxima energies and experimental or known band gaps.

Calculation of thermodynamic stability and electronic band structure

DFT calculations were performed to determine the thermodynamic stabilities and electronic structures of the α-KBiQ₂ and β-KBiQ₂ materials. When compiling the phase diagram for the K–

Bi–S and K–Bi–Se phase spaces in Fig. 8A and B, all the related compounds stored in the Open Quantum Materials Database[51] are considered and the grand canonical linear programming (GCLP) is used to construct the thermodynamic stability convex hull. The energy calculation for the structure of KBi₆.₃₃S₁₀ and its partial occupancies[39] is computationally intensive; thus, the compound is included in the phase diagram assuming it has $T = 0$ K stability. Notably, all ternary phases discovered to date in these phase diagrams lay along the K₂Q–Bi₂Q₃ composition line, including the titular compounds. The intermediate phases, K₃BiS₃ and K₃BiSe₃, are also on the convex hull, and hence are considered thermodynamically stable ground state phases at $T = 0$ K. Our calculations show that the ordered phases, β-KBiS₂ and β-KBiSe₂, are on the convex hull, while the disordered α-KBiS₂ and α-KBiSe₂ structures are 75 and 76 meV per atom above the hull, respectively. This indicates the beta phases are the thermodynamically stable polymorphs, while the alpha phases are metastable. This agrees with the experimental observations as the beta phases are stable at room temperature, while the alpha phases form at high temperature.

The band structures of β-KBiS₂ and β-KBiSe₂ are shown in Fig. 8C and D, respectively. These two materials are indirect band gap semiconductors with calculated band gaps of 1.45 and 1.12 eV for β-KBiS₂ and β-KBiSe₂, respectively, using PBE
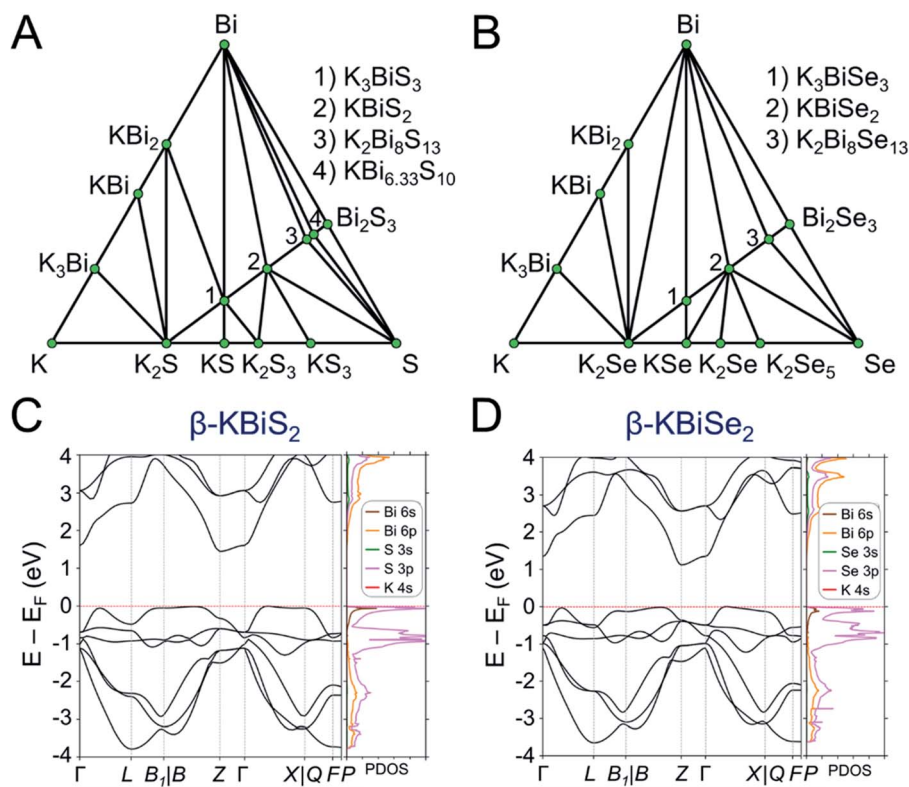
Fig. 8 Phase diagram of (A) K−Bi−S and (B) K−Bi−Se phase space. The band structure and partial density of states (PDOS) of (C) β-KBiS$_2$ ($R\bar{3}m$) and (D) β-KBiSe$_2$ ($R\bar{3}m$).

functional method. These are consistent with the experimental band gaps of 1.55(2) eV and 1.09(2) eV as well as the expectation of the more electronegative sulfur analogue having a wider band gap than the selenium. For both β-KBiQ$_2$ phases, the conduction band minimum is at the Z point of the Brillouin zone, while the valence band maxima are in the region along Γ–L, Z–B and Γ–X directions. The conduction band maximum is primarily comprised of the bismuth 6p$_z$ orbital with contribution from the sulfur 3s orbital (Fig. S10†). The bismuth 6s and sulfur 3p orbitals form the valence band maxima regions (Fig. S10†). The

Γ–L and Γ–X direction have more contribution from the sulfur 3p$_x$ orbital and the bismuth 6s, sulfur 3p$_x$ and 3p$_y$ orbitals, respectively. Overall, the conduction band is far more dispersive than the top of the valence band as shown in Fig. 8C and D, indicating that, in the beta phase, the charge transport of electrons would be far more efficient than that of holes. The partial density of states (PDOS) shows that the relatively flat valence band maxima is a consequence of the localized S/Se p orbitals that make up this band.
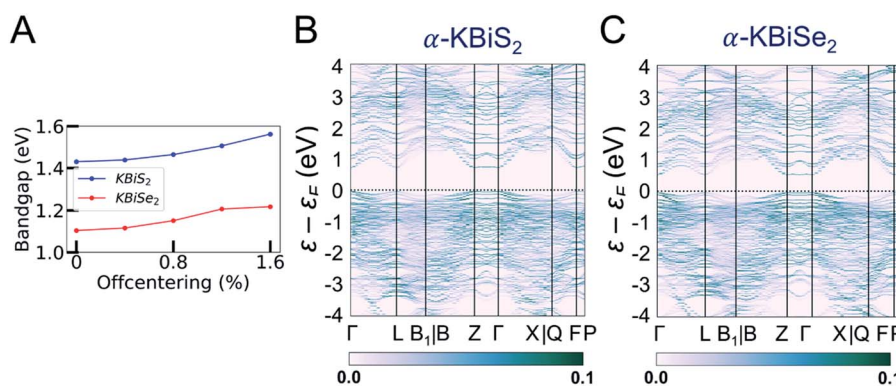

Fig. 9 (A) The DFT-calculated change in band gap as bismuth is increasingly off-centered in the K−Bi−K direction from its ideal position. As described in the Experimental section, the band gaps for α-KBiQ$_2$ (Q = S, Se) are calculated by stacking the rocksalt structure along the [111]-direction to form a supercell and subsequently distributing the cations randomly. While the site distribution is randomized, the distribution is constrained to maintain equivalent amounts of cations. The unfolded band structure of (B) α-KBiS$_2$ and (C) α-KBiSe$_2$, which is unfolded to the Brillouin zone of $R\bar{3}m$ structures. The color bar indicates the band intensity.

In order to understand the electronic structures of the alpha phases, the effects of bismuth off-centering and K/Bi disorder must be separated. The band gaps of the rocksalt-ordered $KBiQ_2$ as a function of coherent bismuth off-centering are shown in Fig. 9A. As the off-centering of bismuth from its ideal positions increases, the band gaps of α-$KBiS_2$ and α-$KBiSe_2$ are calculated to increase. The disordering of α-$KBiQ_2$ is simulated by randomly arranging potassium and bismuth atoms in supercells and the calculated band gaps using the same PBE functional method are 0.77 and 0.58 eV for α-$KBiS_2$ and α-$KBiSe_2$, respectively. The band structures of the alpha phases are shown in Fig. 9B and C. Both dimensional reduction[89] and stereochemical lone pair expression,[84] manifesting as cation ordering (Fig. 7B) and presenting as the off-centering of the bismuth atom, increase the band gap. Therefore, the band gaps of these compounds observed at finite temperature is a combination of these two effects (i.e. increasing the temperature yields a reduction in cation ordering and, on the other hand, an increase in off-centering). The comparative lower value for the experimental band gaps of disordered α-$KBiQ_2$ than those of the ordered β-$KBiQ_2$ materials indicates the influence of ordering has a larger effect than that of off-centering on the band gap, which is consistent with our calculations.

Comparison of A–Bi–Q

When looking at $ABiQ_2$ (A = alkali metal, Q = S, Se, Te) compounds, simultaneous trends of decreasing symmetry and dimensionality are observed as the size of the alkali metal increases relative to bismuth (Fig. 10). As we move across the sulfides in Fig. 10D, the $[BiQ_2]^{1-}$ framework is progressively broken up by the increasingly larger alkali metal illustrated in Fig. 10A–C. This is consistent with the so-called "counterion effect," where, given an anionic framework, a countercation can induce a specific structural change as result of steric effects as a function of its size.[96–99] Previous work[5,97] has shown that the smaller the countercation, the higher the dimensionality and the higher coordination numbers of the metal in the covalent framework.

As the alkali metal increases in size, there is a decrease in dimensionality in agreement with the counterion effect that results from the end of site-sharing for the alkali metal and pnictogen.[96,97] The previously reported lithium, sodium, and potassium $ABiQ_2$ compounds crystallize in the rocksalt structure with the alkali metal and bismuth sharing the same octahedral cation site, shown in Fig. 10A. As observed in this work, $KBiS_2$ and $KBiSe_2$ can be directed to crystallize in the β-phase (Fig. 10B), which is in the α-$NaFeO_2$ structure type. DFT mixing entropy calculations, shown in Fig. S13,† corroborate these experimental results and underscore that the rocksalt structure cannot be stabilized by finite temperature compared to the α-$NaFeO_2$ structure type. This structure consists of $[BiS_2]^-$ layers stacked perpendicular to the c-axis and separated by K^+ cations (Fig. 10B). The potassium ternary marks an inflection point of site-sharing of bismuth and the alkali metal, as the rubidium and cesium ternaries also do not exhibit site-sharing of the two cations. The framework here transitions from a three dimensional covalent framework to a two dimensional layered framework, as highlighted previously in Fig. 7B. $RbBiS_2$ crystallizes in the α-$NaFeO_2$ structure type, similar to β-$KBiS_2$ and β-$KBiSe_2$, where bismuth and potassium separately occupy sites in alternate layers. $RbBiSe_2$ was synthesized using a 1.5 Rb_2-Se : 1 Bi_2Se_3 ratio and is indexed to be in the $R\bar{3}m$ space group.

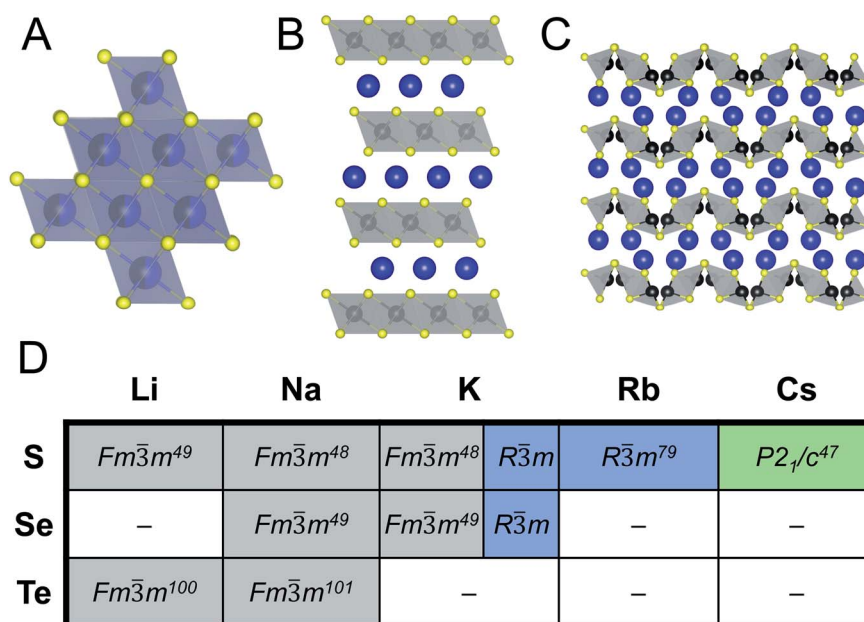|	Li	Na	K	Rb	Cs
S	$Fm\bar{3}m^{49}$	$Fm\bar{3}m^{48}$	$Fm\bar{3}m^{48}$	$R\bar{3}m$	$R\bar{3}m^{79}$	$P2_1/c^{47}$
Se	–	$Fm\bar{3}m^{49}$	$Fm\bar{3}m^{49}$	$R\bar{3}m$	–	–
Te	$Fm\bar{3}m^{100}$	$Fm\bar{3}m^{101}$	–	–	–

Fig. 10 Representative illustrations of $ABiQ_2$ (A = alkali metal, Q = S, Se, Te) structures that crystallize in the (A) rocksalt structure type ($Fm\bar{3}m$), (B) α-$NaFeO_2$ structure type ($R\bar{3}m$), and (C) $CsSbS_2$ structure type ($P2_1/c$). Monovalent cation shown in blue, trivalent cation in black, and chalcogenide in yellow. (D) Chart of $ABiQ_2$ compounds reported in literature[47–49,79,100,101] and in this paper.

$CsBiS_2$ crystallizes in the $CsSbS_2$ structure type ($P2_1/c$), shown in Fig. 10C. This structure exemplifies the transition from a 2D covalent framework to a 1D framework as it comprises extended, corrugated $[BiS_2]^-$ chains separated by Cs^+ atoms.

With potassium acting as an inflection point in the $ABiQ_2$ system, there is a region of stability for six-coordinate site-sharing of bismuth and alkali metal corresponding to a cation radii ratio $\left(\frac{r^+}{r^{3+}}\right)$ of 1.33 or less, using Shannon ionic radii.[102] For ratios higher than 1.33, the cation-ordered structure forms (*e.g.* $RbBiS_2$, $RbBiSe_2$, and $CsBiS_2$). A similar cation radii tolerance is found in the $ALnS_2$[54] and AAn_2Q_6[103] structures (A = alkali metal or Tl, Ln = lanthanide, An = Th, U, Np), thus supporting the plausibility of this proposed site-sharing tolerance. Inspection of antimony analogues corroborates the cation radii tolerance for metal site sharing. $NaSbS_2$ forms in both the rocksalt structure[50] and in the $KSbS_2$ structure type.[104] The $\frac{Na^+}{Sb^{3+}}$ ratio is 1.3, which within approximation agrees with the previous trend for bismuth. $KSbS_2$ crystallizes only in a cation-ordered structure and is not observed in a disordered rocksalt phase; the radius ratio for potassium and antimony $\left(\frac{r^+}{r^{3+}}\right)$ in $KSbS_2$ is 1.8, thereby following the proposed cation radii tolerance.[105]

To demonstrate the robustness of the tolerance factor, the total energies of the three prototypes (Fig. 10A–C) were calculated for all reported structures in Fig. 10D and their accuracy were subsequently compared to the room-temperature structures. The DFT-calculated predictions found that at $T = 0$ K all structures are most stable in the ordered α-$NaFeO_2$ structure type. Notably, the energy difference for $CsBiS_2$ between the rhombohedral and monoclinic structures, as shown in Table S13,† is quite small (≤ 10 meV per atom) at 0 K and, thus, the monoclinic $CsSbS_2$ ($P2_1/c$) structure type is very likely stabilized by temperature. The transition temperature between the rocksalt and α-$NaFeO_2$ structure types, and therefore their temperature dependence, were investigated by introducing ideal mixing entropy (*i.e.* the configurational entropy) to the $T = 0$ K energies and fitting the transition temperatures using the experimental transition temperature of $KBiS_2$. As shown in Table S14,† the calculated transition temperatures follow the disorder-to-order trend predicted by the tolerance factor. The lithium ternaries have a transition temperature below room temperature, indicating that the rocksalt phase would be present at room temperature. The sodium ternaries have similarly low transition temperatures, while the potassium, rubidium, and cesium ternaries have a transition temperature of over ~700 K, thus confirming the robustness of the proposed tolerance factor.

Understanding and employing this proposed cation radii tolerance profitably impacts the numerous fields using ternary chalcogenide semiconductors. More specifically, alkali metal pnictogen chalcogenide ternaries are of interest for thermoelectrics and non-linear optics. In the field of thermoelectrics, binary chalcogenide semiconductors (*i.e.* GeQ, SnQ, PbQ) that crystallize in the rocksalt structure type have historically been of

great interest. Current studies now capitalize on structure–property relationships to optimize properties by exploring solid solutions of rocksalt materials.[44,45] These solid solutions of rocksalt structures reduce the lattice thermal conductivity in the thermoelectric material through phonon scattering as well as exploit band gap engineering. The proposed cation radii ratio $\left(\frac{r^+}{r^{3+}}\right)$, therefore, provides guidance for the compositional requirements to form a cation-disordered $APnQ_2$ ternary (A = alkali metal, Pn = Sb, Bi, Q = S, Se) that may then be mixed with another rocksalt structure. For non-linear optical materials, noncentrosymmetry is a structural requirement. The probability of achieving a noncentrosymmetric space group greatly increases with cation ordering as well as expression of the pnictogen ns^2 lone pair. Therefore, the proposed cation radii ratio can similarly be used to guide cation selection criterion for non-linear optical materials.

Conclusion

In this work, panoramic synthesis is shown to be a valuable tool for materials discovery and mechanistic insight into structure formation of $KBiS_2$ and $KBiSe_2$. Three new compounds were identified, K_3BiS_3, β-$KBiS_2$, and β-$KBiSe_2$. The $KBiQ_2$ however do not form directly. The appearance of K_3BiQ_3 (Q = S, Se) preceding the formation of $KBiQ_2$ suggests that this compound is mechanistically important as an intermediate in the reaction pathway. K_3BiQ_3 serves as a transition point for the potassium coordination environment and for cation intermixing. The observation of the $KBiQ_2$ as both a rocksalt and α-$NaFeO_2$ type structure, while $NaBiQ_2$ and $RbBiQ_2$ crystallize in the $Fm\bar{3}m$ and $R\bar{3}m$ space groups, respectively, suggests that there is a cation radius tolerance $\left(\frac{r^+}{r^{3+}}\right)$ of 1.33 or greater for high symmetry rocksalt formation. Thermal analysis data and DFT calculations show that the cation-ordered polymorphs are the thermodynamically stable phases, while PDF analysis shows that the structures have local off-centering from stereochemically active $6s^2$ lone pair expression on the bismuth. DFT calculations also corroborate the increase in band gap from α-$KBiQ_2$ to β-$KBiQ_2$ as a result of dimensional reduction. By continuing to develop and catalog reactions using *in situ* diffraction techniques, we can work to expand our mechanistic understanding and predictive power towards the ultimate goal of synthesis-by-design.

Author contributions

The idea for this project was conceived by M. G. K. and R. M. The manuscript was written by R. M. and M. G. K. with input from all authors. R. M. conducted all syntheses, structure solutions, and optical characterizations. C. D. M. assisted with optimizing the *in situ* experimental set-up, conducted the Pair Distribution Function (PDF) experiments, and provided fruitful conversations for refinements. J. S. and J. H. ran all DFT calculations under the guidance of C. W. The PDF analyses were

completed by G. B. G. The overall project was supervised by M. G. K.

Conflicts of interest

The authors declare no competing financial interest.

Acknowledgements

References

1 M. Sagawa, S. Fujimura, N. Togawa, H. Yamamoto and Y. Matsuura, *J. Appl. Phys.*, 1984, **55**, 2083–2087.

2 T. E. Schlesinger, J. E. Toney, H. Yoon, E. Y. Lee, B. A. Brunett, L. Franks and R. B. James, *Mater. Sci. Eng., R*, 2001, **32**, 103–189.

3 J. D. Bierlein and H. Vanherzeele, *J. Opt. Soc. Am. B*, 1989, **6**, 622–633.

4 H. P. Maruska and J. J. Tietjen, *Appl. Phys. Lett.*, 1969, **15**, 327–329.

5 I. Chung and M. G. Kanatzidis, *Chem. Mater.*, 2014, **26**, 849–869.

6 T. T. Tran, H. Yu, J. M. Rondinelli, K. R. Poeppelmeier and P. S. Halasyamani, *Chem. Mater.*, 2016, **28**, 5238–5258.

7 M. K. Wu, J. R. Ashburn, C. J. Torng, P. H. Hor, R. L. Meng, L. Gao, Z. J. Huang, Y. Q. Wang and C. W. Chu, *Phys. Rev. Lett.*, 1987, **58**, 908–910.

8 Y. Kamihara, T. Watanabe, M. Hirano and H. Hosono, *J. Am. Chem. Soc.*, 2008, **130**, 3296–3297.

9 K. Mizushima, P. C. Jones, P. J. Wiseman and J. B. Goodenough, *Mater. Res. Bull.*, 1980, **15**, 783–789.

10 A. K. Padhi, K. S. Nanjundaswamy and J. B. Goodenough, *J. Electrochem. Soc.*, 1997, **144**, 1188–1194.

11 L.-D. Zhao, S.-H. Lo, Y. Zhang, H. Sun, G. Tan, C. Uher, C. Wolverton, V. P. Dravid and M. G. Kanatzidis, *Nature*, 2014, **508**, 373.

12 S. R. Ovshinsky, *Phys. Rev. Lett.*, 1968, **21**, 1450–1453.

13 L. Soderholm and J. F. Mitchell, *APL Mater.*, 2016, **4**, 053212.

14 N. Pienack and W. Bensch, *Angew. Chem., Int. Ed. Engl.*, 2011, **50**, 2014–2034.

15 J. R. Chamorro and T. M. McQueen, *Acc. Chem. Res.*, 2018, **51**, 2918–2925.

16 H. Kohlmann, *Eur. J. Inorg. Chem.*, 2019, **2019**, 4174–4180.

17 D.-Y. Chung, K.-S. Choi, L. Iordanidis, J. L. Schindler, P. W. Brazis, C. R. Kannewurf, B. Chen, S. Hu, C. Uher and M. G. Kanatzidis, *Chem. Mater.*, 1997, **9**, 3060–3071.

18 D. P. Shoemaker, Y. J. Hu, D. Y. Chung, G. J. Halder, P. J. Chupas, L. Soderholm, J. F. Mitchell and M. G. Kanatzidis, *Proc. Natl. Acad. Sci. U. S. A.*, 2014, **111**, 10922–10927.

19 A. S. Haynes, C. C. Stoumpos, H. Chen, D. Chica and M. G. Kanatzidis, *J. Am. Chem. Soc.*, 2017, **139**, 10814–10821.

20 A. J. Martinolich, J. A. Kurzman and J. R. Neilson, *J. Am. Chem. Soc.*, 2016, **138**, 11031–11037.

21 A. J. Martinolich and J. R. Neilson, *Chem. Mater.*, 2017, **29**, 479–489.

22 X. Jia, A. Lynch, Y. Huang, M. Danielson, I. Lang'at, A. Milder, A. E. Ruby, H. Wang, S. A. Friedler, A. J. Norquist and J. Schrier, *Nature*, 2019, **573**, 251–255.

23 P. Raccuglia, K. C. Elbert, P. D. F. Adler, C. Falk, M. B. Wenny, A. Mollo, M. Zeller, S. A. Friedler, J. Schrier and A. J. Norquist, *Nature*, 2016, **533**, 73–76.

24 M. G. Kanatzidis, *Inorg. Chem.*, 2017, **56**, 3158–3173.

25 R. I. Walton and D. O'Hare, *Chem. Commun.*, 2000, 2283–2291, DOI: 10.1039/B007795J.

26 A. Bhutani, J. A. Schiller, J. L. Zuo, J. N. Eckstein, L. H. Greene, S. Chaudhuri and D. P. Shoemaker, *Chem. Mater.*, 2017, **29**, 5841–5849.

27 A. J. Martinolich and J. R. Neilson, *J. Am. Chem. Soc.*, 2014, **136**, 15654–15659.

28 A. E. Terry, G. B. M. Vaughan, Å. Kvick, R. I. Walton, A. J. Norquist and D. O'Hare, *Synchrotron Radiat. News*, 2002, **15**, 4–13.

29 S. J. Moorhouse, Y. Wu, H. C. Buckley and D. O'Hare, *Chem. Commun.*, 2016, **52**, 13865–13868.

30 Z. Jiang, A. Ramanathan and D. P. Shoemaker, *J. Mater. Chem. C*, 2017, **5**, 5709–5717.

31 S. S. Bhella, S. P. Shafi, F. Trobec, M. Bieringer and V. Thangadurai, *Inorg. Chem.*, 2010, **49**, 1699–1704.

32 R. J. Lundgren, L. M. D. Cranswick and M. Bieringer, *J. Solid State Chem.*, 2006, **179**, 3599–3606.

33 S. P. Shafi, R. J. Lundgren, L. M. D. Cranswick and M. Bieringer, *J. Solid State Chem.*, 2007, **180**, 3333–3340.

34 J. B. Wiley and R. B. Kaner, *Science*, 1992, **255**, 1093–1097.

35 A. S. Haynes, F. O. Saouma, C. O. Otieno, D. J. Clark, D. P. Shoemaker, J. I. Jang and M. G. Kanatzidis, *Chem. Mater.*, 2015, **27**, 1837–1846.

36 D. Friedrich, M. Schlosser, C. Näther and A. Pfitzner, *Inorg. Chem.*, 2018, **57**, 5292–5298.

37 M. G. Kanatzidis, *Acc. Chem. Res.*, 2005, **38**, 359–368.

38 A. Mrotzek and M. G. Kanatzidis, *Acc. Chem. Res.*, 2003, **36**, 111–119.

39 M. G. Kanatzidis, T. J. McCarthy, T. A. Tanzer, L.-H. Chen, L. Iordanidis, T. Hogan, C. R. Kannewurf, C. Uher and B. Chen, *Chem. Mater.*, 1996, **8**, 1465–1474.

40 L. Iordanidis, P. W. Brazis, C. R. Kannewurf and M. G. Kanatzidis, *MRS Online Proc. Libr.*, 1998, **545**, 65–74.

41 D.-Y. Chung, T. Hogan, P. Brazis, M. Rocci-Lane, C. Kannewurf, M. Bastea, C. Uher and M. G. Kanatzidis, *Science*, 2000, **287**, 1024–1027.

42 D.-Y. Chung, T. P. Hogan, M. Rocci-Lane, P. Brazis, J. R. Ireland, C. R. Kannewurf, M. Bastea, C. Uher and M. G. Kanatzidis, *J. Am. Chem. Soc.*, 2004, **126**, 6414–6428.

43 V. Bazakutsa, N. Gnidash, E. Pod'Yachaya, L. Voinova and N. Kravtsova, *Russ. Phys. J.*, 1991, **34**, 992–996.

44 T. J. Slade, T. P. Bailey, J. A. Grovogui, X. Hua, X. Zhang, J. J. Kuo, I. Hadar, G. J. Snyder, C. Wolverton, V. P. Dravid, C. Uher and M. G. Kanatzidis, *Adv. Energy Mater.*, 2019, **9**, 1901377.

45 T. J. Slade, J. A. Grovogui, S. Hao, T. P. Bailey, R. Ma, X. Hua, A. Guéguen, C. Uher, C. Wolverton, V. P. Dravid and M. G. Kanatzidis, *J. Am. Chem. Soc.*, 2018, **140**, 7021–7031.

46 T. K. Bera, J. I. Jang, J.-H. Song, C. D. Malliakas, A. J. Freeman, J. B. Ketterson and M. G. Kanatzidis, *J. Am. Chem. Soc.*, 2010, **132**, 3484–3495.

47 T. J. McCarthy, S. P. Ngeyi, J. H. Liao, D. C. DeGroot, T. Hogan, C. R. Kannewurf and M. G. Kanatzidis, *Chem. Mater.*, 1993, **5**, 331–340.

48 J. W. Boon, *Recl. Trav. Chim. Pays-Bas*, 1944, **63**, 32–34.

49 G. Gattow and J. Zemann, *Z. Anorg. Allg. Chem.*, 1955, **279**, 324–327.

50 J. Olivier-Fourcade, E. Philippot and M. Maurin, *Z. Anorg. Allg. Chem.*, 1978, **446**, 159–168.

51 J. E. Saal, S. Kirklin, M. Aykol, B. Meredig and C. Wolverton, *JOM*, 2013, **65**, 1501–1509.

52 Y. Peng, Q. Sun, H. Chen and W.-J. Yin, *J. Phys. Chem. Lett.*, 2019, **10**, 4566–4570.

53 J.-P. Sun, G. C. McKeown Wessler, T. Wang, T. Zhu, V. Blum and D. B. Mitzi, *Chem. Mater.*, 2020, **32**, 1636–1649.

54 J. Fabry, L. Havlak, M. Dusek, P. Vanek, J. Drahokoupil and K. Jurek, *Acta Crystallogr., Sect. B: Struct. Sci., Cryst. Eng. Mater.*, 2014, **70**, 360–371.

55 K. Momma and F. Izumi, *J. Appl. Crystallogr.*, 2008, **41**, 653–658.

56 B. H. Toby and R. B. Von Dreele, *J. Appl. Crystallogr.*, 2013, **46**, 544–549.

57 P. Juhas, T. Davis, C. L. Farrow and S. J. L. Billinge, *J. Appl. Crystallogr.*, 2013, **46**, 560–566.

58 C. L. Farrow, P. Juhas, J. W. Liu, D. Bryndin, E. S. Božin, J. Bloch, T. Proffen and S. J. L. Billinge, *J. Phys.: Condens. Matter*, 2007, **19**, 335219.

59 M. I. Aroyo, J. M. Perez-Mato, D. Orobengoa, E. Tasci, G. de la Flor and A. Kirov, *Bulg. Chem. Commun.*, 2011, **43**, 183–197.

60 M. I. Aroyo, A. Kirov, C. Capillas, J. M. Perez-Mato and H. Wondratschek, *Acta Crystallogr., Sect. A: Found. Crystallogr.*, 2006, **62**, 115–128.

61 M. I. Aroyo, J. M. Perez-Mato, C. Capillas, E. Kroumova, S. Ivantchev, G. Madariaga, A. Kirov and H. Wondratschek, *Z. Kristallogr. Cryst. Mater.*, 2006, **221**, 15.

62 P. E. Blöchl, *Phys. Rev. B: Condens. Matter Mater. Phys.*, 1994, **50**, 17953.

63 G. Kresse and D. Joubert, *Phys. Rev. B: Condens. Matter Mater. Phys.*, 1999, **59**, 1758.

64 G. Kresse and J. Furthmüller, *Phys. Rev. B: Condens. Matter Mater. Phys.*, 1996, **54**, 11169.

65 G. Kresse and J. Furthmüller, *Comput. Mater. Sci.*, 1996, **6**, 15–50.

66 J. P. Perdew, K. Burke and M. Ernzerhof, *Phys. Rev. Lett.*, 1996, **77**, 3865.

67 S. Kirklin, J. E. Saal, B. Meredig, A. Thompson, J. W. Doak, M. Aykol, S. Rühl and C. Wolverton, *npj Comput. Mater.*, 2015, **1**, 15010.

68 A. Zunger, S. H. Wei, L. G. Ferreira and J. E. Bernard, *Phys. Rev. Lett.*, 1990, **65**, 353–356.

69 A. Van de Walle, P. Tiwary, M. De Jong, D. Olmsted, M. Asta, A. Dick, D. Shin, Y. Wang, L.-Q. Chen and Z.-K. Liu, *Calphad*, 2013, **42**, 13–18.

70 A. van de Walle, *Calphad*, 2009, **33**, 266–278.

71 P. V. C. Medeiros, S. Stafström and J. Björk, *Phys. Rev. B: Condens. Matter Mater. Phys.*, 2014, **89**, 041407.

72 P. V. C. Medeiros, S. S. Tsirkin, S. Stafström and J. Björk, *Phys. Rev. B: Condens. Matter Mater. Phys.*, 2015, **91**, 041116.

73 O. Glemser and M. Filcek, *Z. Anorg. Allg. Chem.*, 1955, **279**, 321–323.

74 B. Chen, C. Uher, L. Iordanidis and M. G. Kanatzidis, *Chem. Mater.*, 1997, **9**, 1655–1658.

75 R. E. Brandt, V. Stevanović, D. S. Ginley and T. Buonassisi, *MRS Commun.*, 2015, **5**, 265–275.

76 C. Pompe and A. Pfitzner, *Z. Anorg. Allg. Chem.*, 2013, **639**, 296–300.

77 C. West, *Z. Kristallogr. Cryst. Mater.*, 1934, **88**, 97–115.

78 B. Gabrel'yan, A. Lavrentiev, I. Y. Nikiforov and V. Sobolev, *J. Struct. Chem.*, 2008, **49**, 788–794.

79 Y. V. Voroshilov, E. Y. Peresh and M. I. Golovei, *Chem. Informationsdienst*, 1972, **3**, 777–778.

80 G. C. Mather, C. Dussarrat, J. Etourneau and A. R. West, *J. Mater. Chem.*, 2000, **10**, 2219–2230.

81 M. Bianchini, J. Wang, R. J. Clément, B. Ouyang, P. Xiao, D. Kitchaev, T. Shi, Y. Zhang, Y. Wang, H. Kim, M. Zhang, J. Bai, F. Wang, W. Sun and G. Ceder, *Nat. Mater.*, 2020, **19**, 1088–1095.

82 A. R. West, *Solid State Chemistry and its Applications*, Wiley, 2nd edn, 2014.

83 E. Rathore, R. Juneja, S. P. Culver, N. Minafra, A. K. Singh, W. G. Zeier and K. Biswas, *Chem. Mater.*, 2019, **31**, 2106–2113.

84 D. H. Fabini, G. Laurita, J. S. Bechtel, C. C. Stoumpos, H. A. Evans, A. G. Kontos, Y. S. Raptis, P. Falaras, A. Van der Ven, M. G. Kanatzidis and R. Seshadri, *J. Am. Chem. Soc.*, 2016, **138**, 11820–11832.

85 G. Laurita, D. H. Fabini, C. C. Stoumpos, M. G. Kanatzidis and R. Seshadri, *Chem. Sci.*, 2017, **8**, 5628–5635.

86 E. S. Božin, C. D. Malliakas, P. Souvatzis, T. Proffen, N. A. Spaldin, M. G. Kanatzidis and S. J. L. Billinge, *Science*, 2010, **330**, 1660.

87 K. R. Knox, E. S. Bozin, C. D. Malliakas, M. G. Kanatzidis and S. J. L. Billinge, *Phys. Rev. B: Condens. Matter Mater. Phys.*, 2014, **89**, 014102.

88 A. Walsh, D. J. Payne, R. G. Egdell and G. W. Watson, *Chem. Soc. Rev.*, 2011, **40**, 4455–4463.

89 J. Androulakis, S. C. Peter, H. Li, C. D. Malliakas, J. A. Peters, Z. Liu, B. W. Wessels, J.-H. Song, H. Jin, A. J. Freeman and M. G. Kanatzidis, *Adv. Mater.*, 2011, **23**, 4163–4167.

90 *CRC Handbook of Chemistry and Physics*, ed. J. R. Rumble, CRC Press LLC, Boca Raton, FL, 99th edn, 2018.

91 W. Bludau, A. Onton and W. Heinke, *J. Appl. Phys.*, 1974, **45**, 1846–1848.

92 G. Fonthal, L. Tirado-Mejía, J. I. Marín-Hurtado, H. Ariza-Calderón and J. G. Mendoza-Alvarez, *J. Phys. Chem. Solids*, 2000, **61**, 579–583.

93 I. Spanopoulos, I. Hadar, W. Ke, Q. Tu, M. Chen, H. Tsai, Y. He, G. Shekhawat, V. P. Dravid, M. R. Wasielewski, A. D. Mohite, C. C. Stoumpos and M. G. Kanatzidis, *J. Am. Chem. Soc.*, 2019, **141**, 5518–5534.

94 V. Stevanović, S. Lany, D. S. Ginley, W. Tumas and A. Zunger, *Phys. Chem. Chem. Phys.*, 2014, **16**, 3706–3714.

95 H. Tang, H. Berger, P. E. Schmid, F. Lévy and G. Burri, *Solid State Commun.*, 1993, **87**, 847–850.

96 M. G. Kanatzidis, *Phosphorus, Sulfur Silicon Relat. Elem.*, 1994, **93**, 159–172.

97 K.-W. Kim and M. G. Kanatzidis, *J. Am. Chem. Soc.*, 1998, **120**, 8124–8135.

98 Y.-J. Lu and J. A. Ibers, *Comments Inorg. Chem.*, 1993, **14**, 229–243.

99 E. G. Tulsky and J. R. Long, *Chem. Mater.*, 2001, **13**, 1149–1166.

100 A. F. Trippel, V. B. Lazarev and S. I. Berul, *Zh. Neorg. Khim.*, 1978, **23**, 707–710.

101 B. Eisenmann and H. Schäfer, *Z. Anorg. Allg. Chem.*, 1979, **456**, 87–94.

102 R. D. Shannon, *Acta Crystallogr., Sect. A: Cryst. Phys., Diffr., Theor. Gen. Crystallogr.*, 1976, **32**, 751–767.

103 D. E. Bugaris, D. M. Wells, J. Yao, S. Skanthakumar, R. G. Haire, L. Soderholm and J. A. Ibers, *Inorg. Chem.*, 2010, **49**, 8381–8388.

104 K. Cenzual, L. M. Gelato, M. Penzo and E. Parthe, *Acta Crystallogr., Sect. B: Struct. Sci.*, 1991, **47**, 433–439.

105 H. A. Graf and H. Schäfer, *Z. Anorg. Allg. Chem.*, 1975, **414**, 211–219.